INTERNATIONAL JOURNAL FOR NUMERICAL METHODS IN FLUIDS
Int. J. Numer. Meth. Fluids 2005; **48**:649–670
Published online 14 March 2005 in Wiley InterScience (www.interscience.wiley.com). DOI: 10.1002/fld.950

Mathematical modelling of two-phase non-Newtonian flow in a helical pipe

L. Cheng[1,‡], A. V. Kuznetsov[1,*,†] and K. P. Sandeep[2,§]

[1]*Department of Mechanical and Aerospace Engineering, North Carolina State University, Campus Box 7910, Raleigh, NC 27695-7910, U.S.A.*
[2]*Department of Food Science, North Carolina State University, Raleigh, NC, U.S.A.*

SUMMARY

Governing equations for a two-phase 3D helical pipe flow of a non-Newtonian fluid with large particles are derived in an orthogonal helical coordinate system. The Lagrangian approach is utilized to model solid particle trajectories. The interaction between solid particles and the fluid that carries them is accounted for by a source term in the momentum equation for the fluid. The force-coupling method (FCM), developed by M.R. Maxey and his group, is adopted; in this method the momentum source term is no longer a Dirac delta function but is spread on a numerical mesh by using a finite-sized envelop with a spherical Gaussian distribution. The influence of inter-particle and particle–wall collisions is also taken into account. Copyright © 2005 John Wiley & Sons, Ltd.

KEY WORDS: non-Newtonian fluid; two-phase flow; helical pipe; orthogonal helical coordinates; force-coupling method

INTRODUCTION

Because of space saving and, more importantly, the enhancement of mixing achieved due to the secondary flow, helical pipes are widely used in industry. The centrifugal force increases the axial velocity near the pipe outer wall and decreases that near the pipe inner wall. At the pipe outer wall, the higher velocity decreases the thermal resistance considerably, resulting in a higher heat transfer coefficient between the fluid and the pipe wall [1]. Cheng and Kuznetsov [2, 3] numerically investigated heat transfer in a fully developed laminar flow

*Correspondence to: A. V. Kuznetsov, Department of Mechanical and Aerospace Engineering, North Carolina State University, Campus Box 7910, Raleigh, NC 27695-7910, U.S.A.
†E-mail: avkuznet@eos.ncsu.edu
‡E-mail: lcheng@unity.ncsu.edu
§E-mail: kp_sandeep@ncsu.edu

Contract/grant sponsor: USDA

Received 29 October 2004
Revised 24 January 2005
Accepted 27 January 2005

of a non-Newtonian fluid in a helical pipe with the momentum and energy equations derived in an orthogonal helical coordinate system.

Two-phase flow can be modeled by two approaches, the Eulerian/Eulerican and the Eulerian/Lagrangian. In the Eulerian/Eulerican approach, both the solid phase and carrying fluid are treated as continuum phases. This approach is often used to deal with large concentrations of small particles. In the Eulerian/Lagrangian approach, however, only the carrying fluid is described as a continuum and the continuity and momentum equations for the fluid phase are solved on an Eulerian grid. The particle motion is governed by Newton's second law. When particles are moving in the fluid, the momentum is exchanged between the particles and the fluid. This effect is described by a source term introduced into the momentum equation for the fluid phase. This approach has advantages in predicting particle trajectories and is suitable for a low concentration of large particles [1, 4, 5]. The main practical significance of the results of this paper is in predicting the dynamics of large particles in aseptic processing of food, in which information about individual particle trajectories is needed; therefore, the Eulerian/Lagrangian approach is utilized.

The most accurate results in modelling two-phase flow with large particles are obtained by direct numerical simulation of these flows [6, 7]. However, this method is hard to implement and is very costly computationally. This approach is characterized by the need to remesh the domain to accommodate the motion of the particles as well as to map the finite element mesh onto the parallel processors. An alternative numerical strategy utilizes the distributed Lagrange multiplier method [8]. Another numerical method frequently used in the literature utilizes immersed boundary schemes [9, 10]. Maxey *et al.* [11] and Maxey and Patel [12] introduced a forced-coupling method (FCM), the basic idea of which is to model the presence of each particle in the flow by a low-order expansion of finite-valued, force mutlipoles applied as a distributed body force on the flow. Fluid fills the whole domain, including the volume occupied by the particles, and the Navier–Stokes equations with this body force term are solved throughout the domain on a fixed numerical mesh. Based on the fluid flow field, the particle trajectories and velocities are determined. Lomholt and Maxey [13] extended FCM to include higher-order effects by introducing force dipole terms and generalized this approach to bounded domains. To address the collision problem, Glowinski *et al.* [8] adopted a collision strategy described below, which is based on activating an artificial repelling force at a close range.

Aseptic processing of fruit juices and other homogeneous products has been extensively studied. However, few commercial activities for aseptic processing of foods containing large particles have been approved by the Food and Drug Administration (FDA) due to the lack of information regarding the behaviour of large food particles in a flow. This information is the key to determining the residence time distribution (RTD) of particles in the suspension and the heat transfer coefficient between the particles and the fluid, which are the two critical factors in aseptic processing. To ensure that the fastest moving particles get enough thermal treatment and to keep the slower particles from overheating, the residence time distribution must be as narrow as possible. The relative velocity between the solid particles and the fluid has a critical influence on heat transfer as well as on the temperature distribution in the particles. Therefore, the dynamics of the particles and the fluid is the basic information necessary to design a commercially safe and economical aseptic process [4, 14].

In aseptic processing, the carrying fluid, such as milk, soup, sauce or fruit juices, is typically non-Newtonian, so the viscosity of the fluid is different at different locations in the pipe, which further complicates the problem. Sandeep *et al.* [14] made the first attempt to

model non-Newtonian two-phase flows in conventional and helical holding pipes. A Cartesian coordinate system was utilized and the low-order effect of back influence of the particles on the fluid flow was investigated. In this paper, different from Sandeep *et al.* [14], an orthogonal helical coordinate system introduced by Germano [15, 16] is utilized. This allows capturing more accurately the secondary flow in the planes normal to the main flow. The extended FCM method developed by Maxey *et al.* [11–13, 17], with a collision strategy, is applied to describe the effect of particles on the flow field. The non-Newtonian fluid is simulated by the Ostwald-de Waele model [18]. The simulation is based on a fully 3D flow in a helical pipe and the flow field is computed for any moment of time when particles are travelling from the inlet to the outlet of the pipe. In this study, the particles of a spherical shape are considered.

MATHEMATICAL MODELLING

Equations of motion for the fluid with particles

Figure 1(a) depicts a schematic diagram of a helical pipe while Figure 1(b) shows the orthogonal helical coordinate system. The helical pipe can be viewed as a pipe of radius a wound around a cylinder of a constant radius, $R - a$. The parameters that characterize the geometry of a helical pipe include the pipe diameter, $2a$, the coil diameter, $2R$, and the pitch, p. The curvature, κ, and the torsion, τ, are defined as $\kappa = R/(R^2 + p^2)$ and $\tau = p/(R^2 + p^2)$,

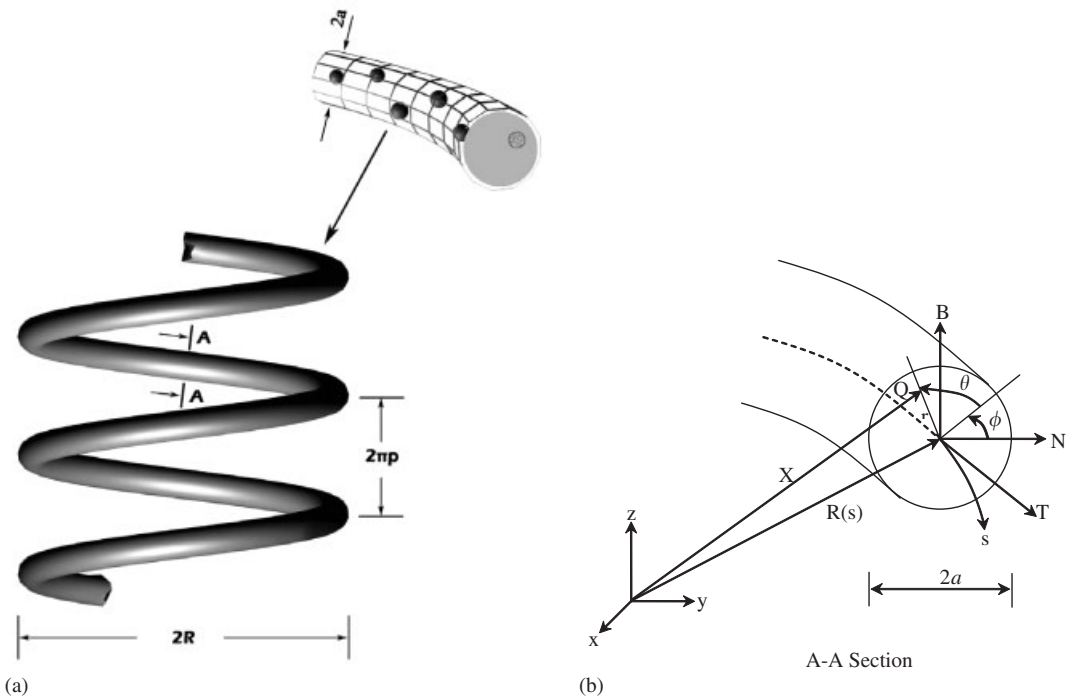

Figure 1. (a) Schematic diagram of a two phase flow in a helical pipe; and (b) the orthogonal helical coordinate system.

respectively. The declining angle of the pipe wounding around the cylinder is

$$\beta = \frac{p}{\sqrt{p^2 + R^2}}$$

The governing equations for a non-Newtonian fluid flow in a helical pipe [2, 3] that account for gravity as well as the influence of particles on the fluid flow are

$$\nabla \cdot \mathbf{v} = 0 \tag{1}$$

$$\rho_f \frac{D\mathbf{v}}{Dt} = -\nabla P + \nabla \cdot \mu \nabla \mathbf{v} + \rho_f \mathbf{g} + \mathbf{f} \tag{2}$$

where $\mathbf{f} = (f_s, f_r, f_\theta)$ represents the momentum transfer resulting from all particles, which is given by the sum of the source terms obtained accounting for the contribution of each particle. The derivation of the momentum source term $\mathbf{f}$ is discussed in detail later on. In the orthogonal helical coordinate system introduced by Germano [15, 16], the scale factors are expressed as

$$h_s = 1 + \kappa r \sin(\theta + \phi), \quad h_r = 1, \quad h_\theta = r \tag{3}$$

and Equations (1) and (2) become

$$\frac{\partial (r u_s)}{\partial s} + \frac{\partial (r h_s u_r)}{\partial r} + \frac{\partial (h_s u_\theta)}{\partial \theta} = 0 \tag{4}$$

$$\begin{aligned}
&\frac{\partial u_s}{\partial t} + \frac{1}{h_s r}\left(\frac{\partial (r u_s u_s)}{\partial s} + \frac{\partial (r h_s u_r u_s)}{\partial r} + \frac{\partial (h_s u_\theta u_s)}{\partial \theta}\right) + \frac{\kappa}{h_s} u_s (u_r \sin(\theta + \phi) + u_\theta \cos(\theta + \phi)) \\
&\quad = -\frac{1}{h_s}\frac{1}{\rho_f}\frac{\partial P}{\partial s} + \frac{\mu}{\rho_f}\left\{\frac{1}{h_s}\frac{\partial}{\partial s}\left[\frac{1}{h_s r}\left[\frac{\partial (r u_s)}{\partial s} + \frac{\partial (r h_s u_r)}{\partial r} + \frac{\partial (h_s u_\theta)}{\partial \theta}\right]\right]\right. \\
&\qquad \left. -\frac{1}{r}\left(\frac{\partial}{\partial r}\left(\frac{r}{h_s}\left(\frac{\partial u_r}{\partial s} - \frac{\partial}{\partial r}(h_s u_s)\right)\right) - \frac{\partial}{\partial \theta}\left(\frac{1}{h_s r}\left(\frac{\partial}{\partial \theta}(h_s u_s) - \frac{\partial}{\partial s}(r u_\theta)\right)\right)\right)\right\} \\
&\qquad + \frac{1}{\rho_f}\left[\frac{1}{h_s^2}\frac{\partial u_s}{\partial s}\frac{\partial \mu}{\partial s} + \frac{\partial u_s}{\partial r}\frac{\partial \mu}{\partial r} + \frac{1}{r^2}\frac{\partial u_s}{\partial \theta}\frac{\partial \mu}{\partial \theta}\right] \\
&\qquad - g \sin\beta + f_s/\rho_f
\end{aligned} \tag{5a}$$

$$\begin{aligned}
&\frac{\partial u_r}{\partial t} + \frac{1}{h_s r}\left(\frac{\partial (r u_s u_r)}{\partial s} + \frac{\partial (r h_s u_r u_r)}{\partial r} + \frac{\partial (h_s u_\theta u_r)}{\partial \theta}\right) - \frac{u_\theta^2}{r} - \frac{k}{h_s} u_s^2 \sin(\theta + \phi) \\
&\quad = -\frac{1}{\rho_f}\frac{\partial P}{\partial r} + \frac{\mu}{\rho_f}\left\{\frac{\partial}{\partial r}\left[\frac{1}{h_s r}\left[\frac{\partial (r u_s)}{\partial s} + \frac{\partial (r h_s u_r)}{\partial r} + \frac{\partial (h_s u_\theta)}{\partial \theta}\right]\right]\right. \\
&\qquad \left. -\frac{1}{h_s r}\left(\frac{\partial}{\partial \theta}\left(\frac{h_s}{r}\left(\frac{\partial}{\partial r}(r u_\theta) - \frac{\partial u_r}{\partial \theta}\right)\right) - \frac{\partial}{\partial s}\left(\frac{r}{h_s}\left(\frac{\partial u_r}{\partial s} - \frac{\partial}{\partial r}(h_s u_s)\right)\right)\right)\right\}
\end{aligned}$$

$$+\frac{1}{\rho_f}\left[\frac{1}{h_s^2}\frac{\partial u_r}{\partial s}\frac{\partial \mu}{\partial s}+\frac{\partial u_r}{\partial r}\frac{\partial \mu}{\partial r}+\frac{1}{r^2}\frac{\partial u_r}{\partial \theta}\frac{\partial \mu}{\partial \theta}\right]$$
$$-g\cos\beta\sin(\theta+\phi)+f_r/\rho_f \tag{5b}$$

$$\frac{\partial u_\theta}{\partial t}+\frac{1}{h_s r}\left(\frac{\partial(ru_s u_\theta)}{\partial s}+\frac{\partial(rh_s u_r u_\theta)}{\partial r}+\frac{\partial(h_s u_\theta u_\theta)}{\partial \theta}\right)-\frac{\kappa}{h_s}u_s^2\cos(\theta+\phi)+\frac{u_r u_\theta}{r}$$
$$=-\frac{1}{r}\frac{1}{\rho_f}\frac{\partial P}{\partial \theta}+\frac{\mu}{\rho_f}\left\{\frac{1}{r}\frac{\partial}{\partial \theta}\left[\frac{1}{h_s r}\left[\frac{\partial(ru_s)}{\partial s}+\frac{\partial(rh_s u_r)}{\partial r}+\frac{\partial(h_s u_\theta)}{\partial \theta}\right]\right]\right.$$
$$\left.-\frac{1}{h_s}\left(\frac{\partial}{\partial s}\left(\frac{1}{h_s r}\left(\frac{\partial}{\partial \theta}(h_s u_s)-\frac{\partial}{\partial s}(ru_\theta)\right)\right)-\frac{\partial}{\partial r}\left(\frac{h_s}{r}\left(\frac{\partial}{\partial r}(ru_\theta)-\frac{\partial u_r}{\partial \theta}\right)\right)\right)\right\}$$
$$+\frac{1}{\rho_f}\left[\frac{1}{h_s^2}\frac{\partial u_\theta}{\partial s}\frac{\partial \mu}{\partial s}+\frac{\partial u_\theta}{\partial r}\frac{\partial \mu}{\partial r}+\frac{1}{r^2}\frac{\partial u_\theta}{\partial \theta}\frac{\partial \mu}{\partial \theta}\right]$$
$$-g\cos\beta\cos(\theta+\phi)+f_\theta/\rho_f \tag{5c}$$

The following expression for the effective viscosity of a power law fluid is used to evaluate the viscosity of a non-Newtonian fluid:

$$\mu=m[\tfrac{1}{2}(\Delta:\Delta)]^{(n-1)/2} \tag{6}$$

where Δ is the rate of deformation tensor and the expression for $(\Delta:\Delta)$ is given by

$$\frac{1}{2}(\Delta:\Delta)=2\left[\left(\frac{\partial}{\partial s}\left(\frac{u_s}{h_s}\right)-\frac{\tau\kappa r\cos(\theta-\tau s)}{h_s^2}u_s+\frac{\kappa\sin(\theta-\tau s)}{h_s}u_r+\frac{\kappa\cos(\theta-\tau s)}{h_s}u_\theta\right)^2\right.$$
$$\left.+\left(\frac{\partial u_r}{\partial r}\right)^2+\left(\frac{\partial}{\partial \theta}\left(\frac{u_\theta}{r}\right)+\frac{u_r}{r}\right)^2\right]+\left(h_s\frac{\partial}{\partial r}\left(\frac{u_s}{h_s}\right)+\frac{1}{h_s}\frac{\partial u_r}{\partial s}\right)^2$$
$$+\left(\frac{h_s}{r}\frac{\partial}{\partial \theta}\left(\frac{u_s}{h_s}\right)+\frac{r}{h_s}\frac{\partial}{\partial s}\left(\frac{u_\theta}{r}\right)\right)^2+\left(r\frac{\partial}{\partial r}\left(\frac{u_\theta}{r}\right)+\frac{1}{r}\frac{\partial u_r}{\partial \theta}\right)^2 \tag{7}$$

Momentum source term induced by particles

A force-coupling method (FCM) developed by Maxey *et al.* [11–13, 17] is utilized to simulate the source term incorporated into the momentum equation to account for the presence of the particles. The general principle of FCM is to utilize a localized body force $\mathbf{f}(\mathbf{x},t)$, which is a resultant force of all particles, to represent the effect of the particles on the fluid. The momentum source term is no longer a Dirac delta function but is spread on the numerical mesh by using a finite-sized envelop with a spherical Gaussian distribution. The equations for fluid motion are also solved in the domain occupied by the particles.

The body force generated by N spherical particles centred at $\mathbf{Y}^{(n)}(t)$ $(n=1,2,\ldots,N)$ is

$$\mathbf{f}(\mathbf{x},t)=\sum_{n=1}^{N}\left[\mathbf{F}^{(n)}\Delta(\mathbf{x}-\mathbf{Y}^{(n)}(t))+\mathbf{G}_{ij}^{(n)}\frac{\partial}{\partial x_j}\Delta'(\mathbf{x}-\mathbf{Y}^{(n)}(t))\right] \tag{8}$$

where both $\Delta(x)$ and $\Delta'(x)$ are Gaussian functions:

$$\Delta(x)=(2\pi\sigma^2)^{-3/2}\exp(-r^2/2\sigma^2) \quad \text{with } r=|x| \tag{9}$$

The length scale, σ, for $\Delta(x)$ is set in terms of the particle radius, a_p, as

$$\sigma=\frac{a_\mathrm{p}}{\sqrt{\pi}} \tag{10}$$

The length scale σ' for the second envelop, Δ', is set as

$$\sigma'=\frac{a_\mathrm{p}}{(6\sqrt{\pi})^{1/3}} \tag{11}$$

It should be noted that the existing formulation of FCM is derived for Newtonian fluids; the utilization of this method for a power-law fluid is an approximation utilized in this paper; in particular, length scales given by Equations (10) and (11) are strictly derived for Newtonian fluids only.

The first term in the brackets on the right-hand side of Equation (8) refers to a force monopole, $\mathbf{F}^{(n)}$, for the nth particle, which physically equals to the hydrodynamic drag on the nth particle. The second term in the brackets on the right-hand side refers to a force dipole, $\mathbf{G}_{ij}^{(n)}$, for the nth particle. The strength of the force monopole is determined by the sum of the external force $\mathbf{F}^{(n)^{\mathrm{ext}}}$ acting on the particles and the inertia of the particle:

$$\mathbf{F}^{(n)}=\mathbf{F}^{(n)^{\mathrm{ext}}}-(m_\mathrm{p}^{(n)}-m_\mathrm{f})\frac{\mathrm{d}\mathbf{v}_\mathrm{p}^{(n)}}{\mathrm{d}t} \tag{12}$$

where $\mathbf{v}_\mathrm{p}^{(n)}(t)$ is the particle velocity, which is calculated by averaging the fluid velocity over the region D_p occupied by the particle:

$$\mathbf{v}_\mathrm{p}^{(n)}(t)=\int_{D_\mathrm{p}}\mathbf{v}(\mathbf{x},t)\Delta(\mathbf{x}-\mathbf{Y}^{(n)}(t))\,\mathrm{d}^3\mathbf{x} \tag{13}$$

The only external force $\mathbf{F}^{\mathrm{ext}}$ acting on the particles suspended in the fluid is the buoyancy force. There is no need to include various fluid forces acting on a particle (such as the Magnus and Saffman lift forces or the drag force) since there forces are all internal to the flow system and their influence is captured directly by the simulations.

The buoyancy force exerted on a particle can be computed as:

$$F_{\mathrm{b}} = (4/3)\pi a_{\mathrm{p}}^3(\rho_{\mathrm{f}} - \rho_g)\mathbf{g} \tag{14}$$

In the helical coordinate system, the above forces sum up to the following equations for the s, r, and θ projections of the total external force on the particles:

$$F_s = \tfrac{4}{3}\pi a^3(\rho_{\mathrm{f}} - \rho_{\mathrm{p}})g \sin\beta \tag{15a}$$

$$F_r = \tfrac{4}{3}\pi a^3(\rho_{\mathrm{f}} - \rho_{\mathrm{p}})g \sin\beta \sin\theta \tag{15b}$$

$$F_\theta = \tfrac{4}{3}\pi a^3(\rho_{\mathrm{f}} - \rho_{\mathrm{p}})g \sin\beta \cos\theta \tag{15c}$$

In addition, to prevent particles from overlapping each others domains or penetrating into the wall, an additional inter-particle and particle–wall external short-range repulsive force $\mathbf{F}'$ is added to the force $\mathbf{F}$ for each particle, as suggested by Glowinski *et al.* [8]:

$$\mathbf{F}'^{(n)} = \sum_{n=1, m\neq n}^{N} \mathbf{F}^{P(n,m)} + \mathbf{F}^{\mathrm{w}(n)} \tag{16}$$

The first term on the right-hand side of Equation (16) represents the force exerted on the nth particle by the $N-1$ other particles and the second term represents that exerted by the pipe wall. The particle–particle force is calculated as follows:

$$\mathbf{F}^{P^{(n,m)}} = \begin{cases} 0, & d^{(n,m)} \geqslant a_{\mathrm{p}}^{(n)} + a_{\mathrm{p}}^{(m)} + \delta \\ \dfrac{1}{\varepsilon_{\mathrm{P}}}(\mathbf{Y}^{(n)} - \mathbf{Y}^{(m)})(a_{\mathrm{p}}^{(n)} + a_{\mathrm{p}}^{(m)} + \delta - d^{(n,m)})^2, & d^{(n,m)} \leqslant a_{\mathrm{p}}^{(n)} + a_{\mathrm{p}}^{(m)} + \delta \end{cases} \tag{17}$$

where $d^{(n,m)} = |\mathbf{Y}^{(n)} - \mathbf{Y}^{(m)}|$ is the distance between the centres of the nth and mth particles, $a_{\mathrm{p}}^{(n)}$ is the radius of the nth particle, and ε_{P} is a small positive stiffness parameter. In Equation (17), δ is the force range, which is the distance between the surfaces of two particles (measured along the line that connects their centres) at which the contact force is activated; δ is set to one mesh size in this paper. The particle–wall force is modelled as the force between a particle and the imaginary particle located on the other side of the wall Γ (a mirror image of the particle with respect to the wall) (see Figure 2(a)):

$$\mathbf{F}^{\mathrm{w}^{(n)}} = \begin{cases} 0, & d^{(n)'} \geqslant 2a_{\mathrm{p}}^{(n)} + \delta \\ \dfrac{1}{\varepsilon_{\mathrm{w}}}(\mathbf{Y}^{(n)} - \mathbf{Y}^{(n)'})(2a_{\mathrm{p}}^{(n)} + \delta - d^{(n)'})^2, & d^{(n)'} \leqslant 2a_{\mathrm{p}}^{(n)} + \delta \end{cases} \tag{18}$$

where $d^{(n)'} = |\mathbf{Y}^{(n)} - \mathbf{Y}^{(n)'}|$ is the distance between the centres of the nth particle and the centre of its mirror image, $\mathbf{Y}^{(n)'}$ is the position of the imaginary particle, and ε_{w} is another stiffness parameter. The stiffness parameters are taken as $\varepsilon_{\mathrm{p}} = 8.15 \times 10^{-5}\ \mathrm{m^3\ N^{-1}}$ and $\varepsilon_{\mathrm{w}} = \varepsilon_{\mathrm{p}}/2$.

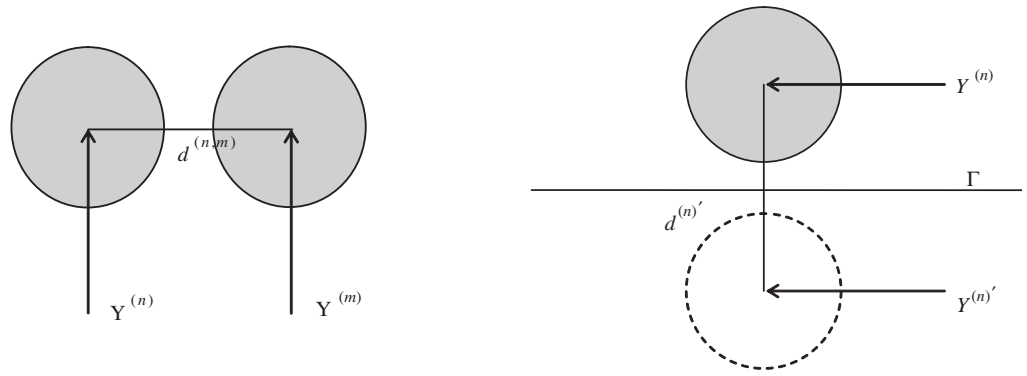

(a)

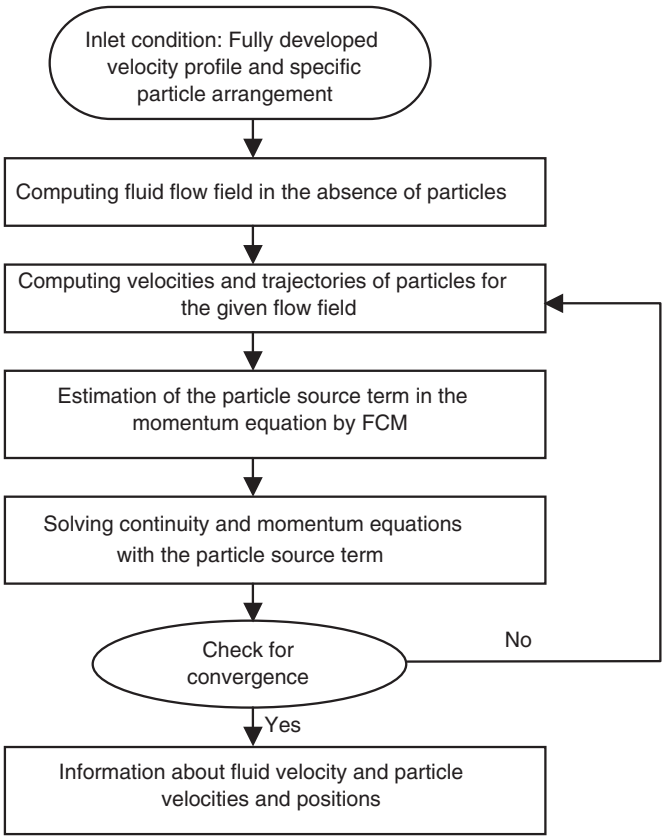

(b)

Figure 2. (a) Schematic diagram for calculating contact forces of inter-particle and particle–wall collisions; and (b) Flowchart of the overall computational algorithm.

Similarly to the velocity, the angular velocity of the nth particle is calculated as follows:

$$\mathbf{\Omega}_{\mathrm{p}}^{(n)} = \frac{1}{2}\int_{D_{\mathrm{p}}} \boldsymbol{\omega}^{(n)}(\mathbf{x},t)\Delta'(\mathbf{x})\,\mathrm{d}^3\mathbf{x} \tag{19}$$

The force dipole, $\mathbf{G}_{ij}^{(n)}$, in Equation (8), which is introduced to improve the flow representation, consists of a symmetric part and an anti-symmetric part. The anti-symmetric part of $\mathbf{G}_{ij}^{(n)}$ is related to the external torque on the particle, and since the moment of inertia of the particles is neglected, the anti-symmetric part of the force dipole is neglected. The algorithm for computing the symmetric part of $\mathbf{G}_{ij}^{(n)}$ (the stresslet) involves the solution of a $5N \times 5N$ liner system and is given in Appendix A of Dance and Maxey [19].

COMPUTATIONAL PROCEDURE

To solve a 3D flow problem, three velocity components at the inlet and the pressure at the outlet must be specified. In this paper, a fully developed velocity profile is specified as the inlet profile of the fluid to the helical pipe. A no-slip boundary condition is specified at the wall of the pipe.

A uniform mesh is generated on an evenly spaced grid in the axial, radial, and circumferential directions. An implicit time-integration scheme and the time marching procedure introduced by Patankar and Spalding [20] is adopted to solve the continuity and momentum equations. The SIMPLE algorithm is utilized on a staggered grid and the longitudinal and cross-stream pressure gradients are uncoupled. The discretized equations are solved iteratively by successive applications of the TDMA (tri-diagonal matrix algorithm).

The continuity and momentum equations (Equations (4) and (5a–c)) for the fluid phase are first solved in the absence of particles. Once the information about the fluid phase motion is obtained, the linear velocities of the particles are determined from Equation (13). The source term defined by Equation (8), which accounts for the influence of particles on the fluid, is calculated using the force-coupling method. The continuity and momentum equations are then solved again taking the particle source term into account, and the procedure is repeated until the following convergence criterion is met:

$$\frac{\|\hat{\mathbf{r}}^{(k)}\|_\infty}{\|U_{s,\mathrm{f}}\|_\infty} \leqslant 10^{-5} \tag{20}$$

where $\hat{\mathbf{r}}$ is the residual of the pressure correction equation obtained from the continuity equation when using the SIMPLE method. The superscript (k) refers to the kth iteration. $U_{s,\mathrm{f}}$ is the mean flow velocity. After the particle velocities are obtained from Equation (13) at a specific moment of time, the displacements of particles are computed at this time step. The flowchart of the overall computational algorithm is shown in Figure 2(b).

Computations were performed on a NCSU supercomputer using a single 208 Intel Xeon 3.0 GHz processor. A typical CPU to investigate the process between the moment when the particles are released and the moment when the particles exit the pipe for a $51 \times 21 \times 21$ uniform mesh with a time step of 0.025 s is about 360 h (when the mean flow velocity is $0.5\,\mathrm{m\,s^{-1}}$).

RESULTS AND DISCUSSION

In this paper, a helical pipe whose length is 1m and whose diameter is 5.08 cm, built by coiling the tube around a cylindrical mandrel (whose diameter is 60 cm) is considered; the pitch of the helical pipe is 2 cm. At the inlet, a fully developed parabolic axial velocity profile is imposed, the radial and circumferential velocity components are assumed to be zero. The uniform atmospheric pressure at the outlet of the pipe is specified. The particles are assumed to be spherical with a diameter of 0.8 cm. The density of the particles is assumed to be the same as that of the fluid. Nine particles are initially introduced at the pipe inlet as fixed obstacles (they initially have zero velocities). The flow in the whole pipe attains steady-state, and then, at $t = 0$ s, the particles are suddenly released, and the cluster of nine particles propagates through the pipe. This makes the flow unsteady, depending on the positions of the particles which are now carried by the fluid. In this study, two cases, A and B, of particle configuration at the inlet are investigated. For Case A, the particles are placed at the inlet with the same radial position (half of the pipe radius) and the same angle between neighboring particles, as shown in Figure 3(A). For Case B, the particles are placed at the inlet with the same angular interval between them (as in Case A), but at different radial positions, as shown in Figure 3(B). The interaction between the particles and the flow field is reciprocal. Both the effect of the particles on the fluid flow and the effects of the flow velocity and different positioning of particles at the inlet of the pipe on particle trajectories and the residence time distribution are investigated.

When there are no particles in the fluid, the maximum of the axial velocity is displaced from the pipe axis to the wall. The secondary flow induces mixing in the fluid. The phenomena of the displacement of the axial velocity and the occurrence of the secondary flow are discussed in detail in Cheng and Kuznetsov [2, 3]. When particles are travelling in the fluid, the impact of the particles on the fluid changes the flow field. First, the case in which the centreline velocity of 1.0 m s^{-1} and the mean velocity of 0.5 m s^{-1} (Case A1) is investigated. To show the fluid flow and the trajectories of the particles, the helical pipe is stretched and viewed from an axial cut view. Figure 4(a) shows the contour lines of the fluid axial velocity when

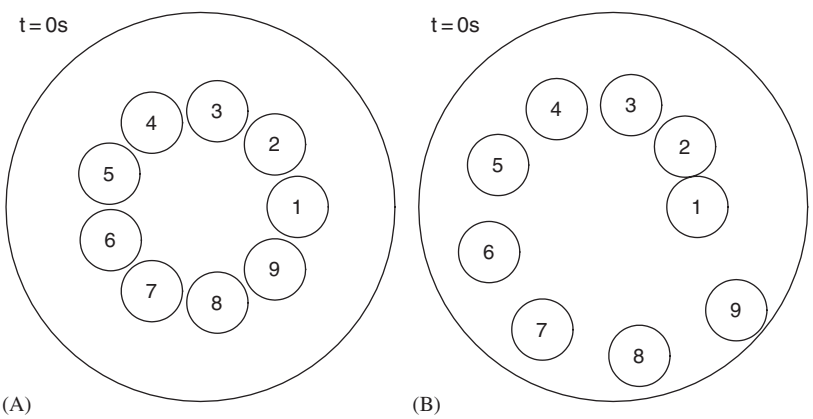

Figure 3. Initial positions of particles at the pipe inlet (Cases A and B).

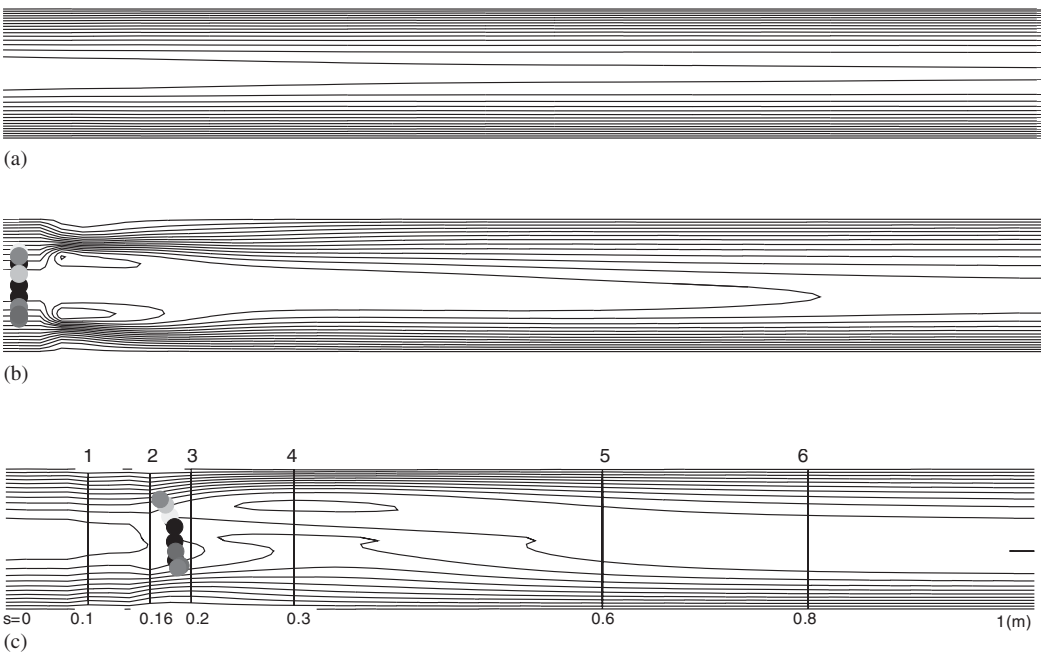

Figure 4. Contour lines of the axial velocity of the fluid flow in the axial cut view of the pipe for: (a) no particles introduced at the inlet; (b) $t = 0.025$ s (particles are close to the inlet); and (c) $t = 0.3$ s (particles are between cross-sections 2 and 3.

no particles are introduced at the inlet of the pipe while Figures 4(b) and 4(c) show the case with particles. Figure 4(b) shows the contour lines of the fluid axial velocity when the particles have just entered the pipe ($t = 0.025$ s). Figure 4(c) shows those when the particles have traveled for 0.3 s and are concentrated between cross-sections 2 and 3. Figure 4(b) shows that vortices have developed close to the pipe inlet due to the presence of the particles. This is because the particles were introduced to the inlet of the pipe as fixed obstacles, and then suddenly released at $t = 0$. It also shows that the vortices are not symmetric, which happens because the pipe is not straight but a helical one. The parabolic distribution of the axial velocity gets deformed as the distance of the cross-section from the inlet increases and the maximum of the axial velocity gets displaced to the outer wall. When the particles are between cross-sections 2 and 3 (Figure 4(c)), the contour lines of the axial velocity clearly show that the particles create a disturbance in the flow field.

To show the influence of the particles on the fluid flow, the axial velocity and the secondary flow for Case A1 in cross-sections 1–6 (the positions of these cross-sections are displayed in Figure 4(c) at $t = 0.3$ s (at this moment of time, the particles are between cross-sections 2 and 3), are presented in Figure 5. In cross-section 1, since it is close to the inlet, the parabolic profile of the axial velocity is not deformed significantly and the secondary flow is also not strong. The particles have just passed cross-section 2. The vector plot of the secondary flow at cross-section 2 shows that the passing of particles through this cross-section increased the strength of the secondary flow and caused an irregular distribution of the axial velocity.

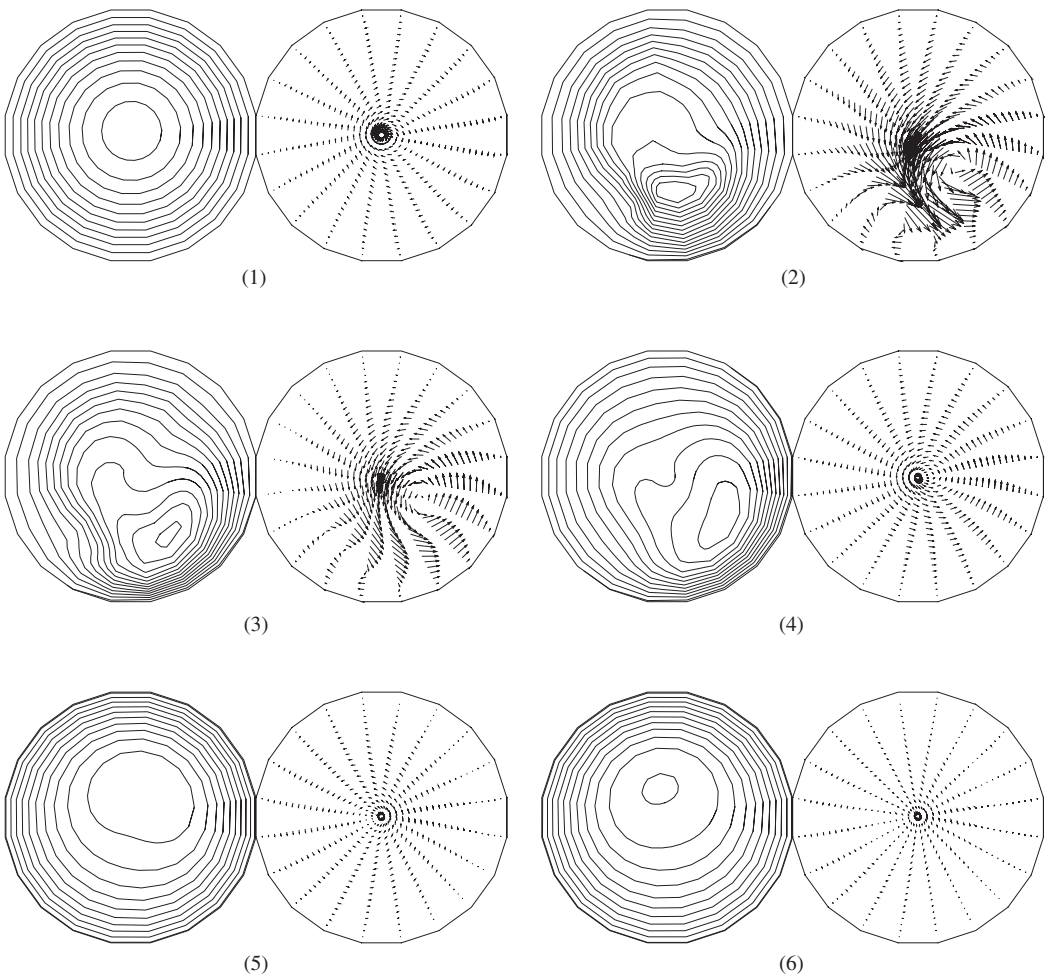

Figure 5. Contour lines of the axial velocity (left) and vector plots of the secondary flow (right) in the cross-sections 1–6 at $t = 0.3$ s, the positions of these cross-sections are displayed in Figure 4(c) (Case A1).

The particles most strongly influence the flow in the cross-section in which the particles are passing at a given moment of time. The deformation of the axial velocity distribution and strengthening of the secondary flow are still significant in cross-section 3 but less than those in cross-section 2 because the particles have not yet reached cross-section 3. The effect of the particles on the flow can be observed in cross-section 4 from the contour lines of the axial velocity but it is not apparent in the vector plots of the secondary flow. However, when a cross-section is located too far downstream from the particles (cross-sections 5 and 6), the effect of the particles becomes negligible.

Figures 6 and 7 depict the axial and radial positions of the particles at different moments of time for Case A1 (in Figure 6, particle positions are projected on the axial cut view

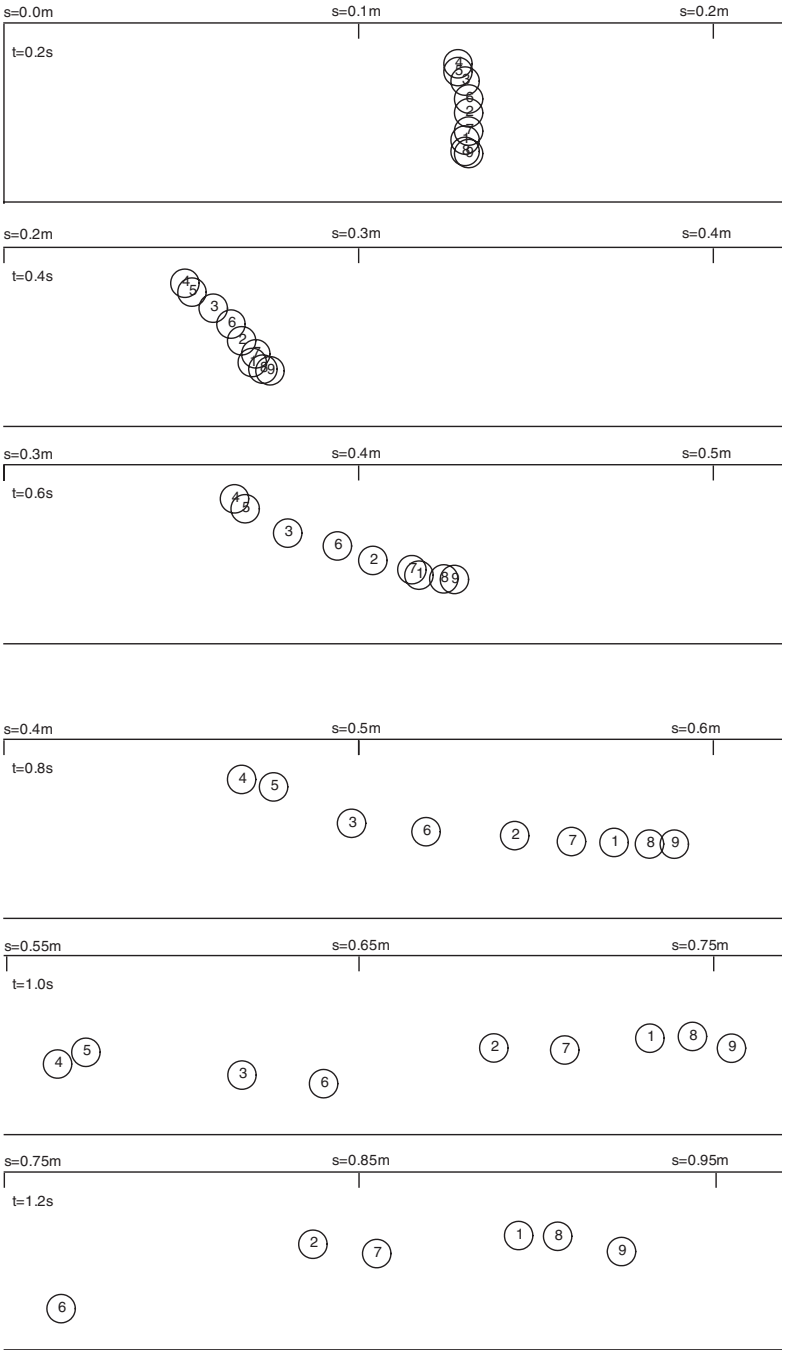

Figure 6. Snapshots of the particles at different moments of time (Case A1).

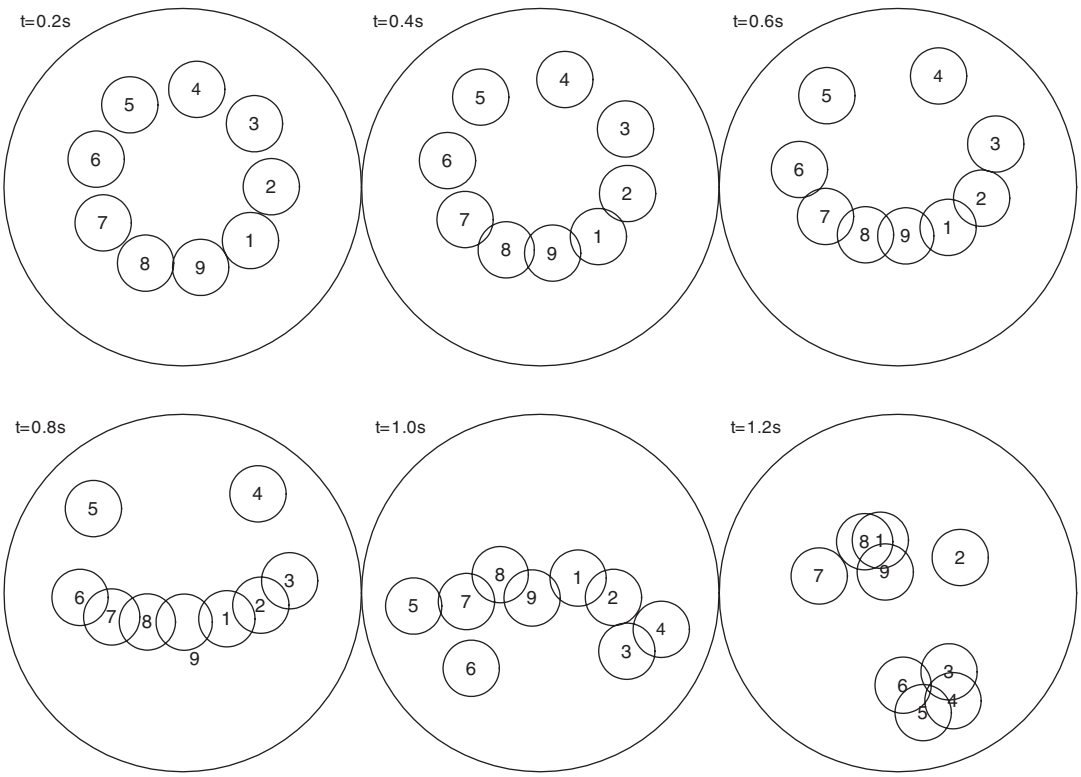

Figure 7. Radial positions of the particles at different moments of time (Case A1).

of the pipe). In the beginning, the axial velocity profile of the fluid flow remains close to parabolic. Since for this case the particles are initially introduced in the same radial positions at the inlet, once they are released, they enter the pipe parallel to each other and the layout of the particles does not change significantly during the first 0.2 s (see Figures 6 and 7 for $t = 0.2$ s). However, the deformed axial velocity distribution and the secondary flow induced by the helical pipe soon cause the particles to move away from each other. The factors that affect the particle trajectories include the local velocity of the fluid flow, the particle inertia as well as particle–particle and particle–wall interactions. Figure 8 displays the projections of the particle trajectories on an axial cut view of the pipe while Figure 9 depicts the axial velocities of the particles versus their axial positions. Both Figures 8 and 9 are computed for Case A1. In the beginning, all particles travel parallel with each other with the same axial velocity. At $s = 0.05$ m, the particle trajectories start overlapping. At $s = 0.57$ m, a 'mixing event' occurs. Figure 9 shows that once the particles are released, they first accelerate (the inertia of the particles is accounted for) and attain the same axial velocity within a very short time and very short distance from the inlet. The acceleration period of the particles is shown on an enlarged scale in a small separate figure in Figure 9. The decrease of the axial velocity of the particles, which follows the acceleration period, may be caused by moving the particles to different radial positions. After approximately 0.1 s, the secondary flow begins to

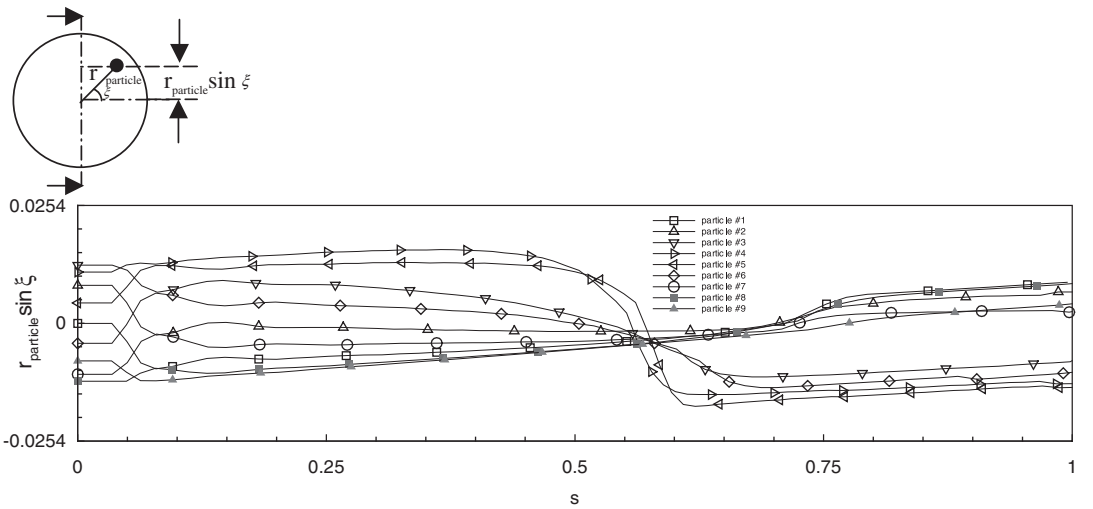

Figure 8. Trajectories of the particles viewed in the axial cut view (Case A1).

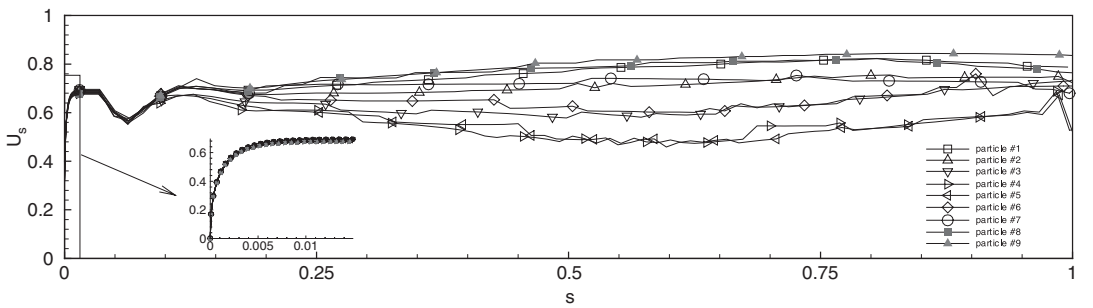

Figure 9. Axial velocities of the particles in the pipe versus their axial positions (Case A1).

show visible influence and the particles move to different radial positions which correspond to different axial velocities.

To investigate the effect of the mean flow velocity on the residence time distribution (RTD) of the particles in the pipe, the inlet configuration of Case A, in which nine particles are introduced at the same inlet radial positions, is computed for three more cases with different mean flow velocities (Cases A2, A3 and A4, respectively). The average axial velocity and the residence time of the particles are listed in Table I. It is shown that the mean, minimum, maximum, and standard deviation of the particle residence time (RT_{mean}, RT_{min}, RT_{max}, and RT_{std}, respectively) are significantly affected by the mean flow velocity. As expected, particles travel faster when the mean flow velocity is increased. The increase of a standard deviation means a more scattered residence time distribution of the particles, which shows that the effect of the secondary flow on the particles is more significant when the fluid axial velocity is small. It can be explained as follows: when the fluid axial velocity increases, the increase

Table I. Axial velocity and residence time of particles introduced to the inlet of the pipe at the same inlet radial positions, computed for different mean flow velocities, $U_{s,\mathrm{f}}$.

Particle	$U_{s,\mathrm{f}} = 0.50\,\mathrm{m\,s^{-1}}$ (A1)		$U_{s,\mathrm{f}} = 0.30\,\mathrm{m\,s^{-1}}$ (A2)		$U_{s,\mathrm{f}} = 0.20\,\mathrm{m\,s^{-1}}$ (A3)		$U_{s,\mathrm{f}} = 0.10\,\mathrm{m\,s^{-1}}$ (A4)	
No.	$U_{s,\mathrm{p}}(\mathrm{m\,s^{-1}})$	RT(s)	$U_{s,\mathrm{p}}(\mathrm{m\,s^{-1}})$	RT(s)	$U_{s,\mathrm{p}}(\mathrm{m\,s^{-1}})$	RT(s)	$U_{s,\mathrm{p}}(\mathrm{m\,s^{-1}})$	RT(s)
1	0.75	1.33	0.50	2.30	0.308	3.25	0.154	6.47
2	0.69	1.46	0.47	2.12	0.283	3.59	0.144	7.04
3	0.63	1.58	0.42	2.39	0.259	3.95	0.131	7.75
4	0.55	1.80	0.37	2.73	0.256	3.58	0.128	7.89
5	0.55	1.83	0.35	2.83	0.260	3.55	0.131	7.04
6	0.65	1.53	0.41	2.49	0.313	3.18	0.155	6.42
7	0.68	1.45	0.47	2.17	0.328	3.01	0.162	6.11
8	0.76	1.33	0.50	2.02	0.327	3.01	0.162	6.06
9	0.77	1.25	0.51	1.97	0.321	3.07	0.160	6.17
$\mathrm{RT_{mean}}$		1.50		2.33		3.35		6.77
$\mathrm{RT_{min}}$		1.83		1.97		3.01		6.06
$\mathrm{RT_{max}}$		1.25		2.83		3.95		7.89
$\mathrm{RT_{std}}$		0.20		0.30		0.33		0.70

of the secondary flow does not keep up with the increase of the axial velocity. This result is in agreement with experimental findings of Tanyel [21].

To investigate the effect of the inlet radial position of particles on their residence time distribution, Case B (in which the particles are introduced at different inlet radial positions) is computed using the same mean flow velocity as was used in Case A1. Figure 10 displays the snapshots of the particles in the pipe for different moments of time (as in Figures 6 and 8, particle positions are projected on the axial cut view of the pipe). It can be seen that the particles have already moved away from each other at $t = 0.2$ s, while for Case A1 all nine particles still stay together (see Figure 6, $t = 0.2$ s). This is because in Case B the particles have different streamwise velocities according to their radial positions. For $t = 0.2$ s, the distribution of the particles takes the shape of an inclined 'S'. This shape remains when t is increased to 0.4 s and even to 0.6 s; however, the particles move away from each other even further. When time reaches 0.8 s, particle 6 catches up to particle 5 and the S-shape is deformed. After this point, the deformed axial velocity distribution and the secondary flow in the helical pipe make the particle distribution even more deformed. This phenomenon can also be observed in Figure 11, which depicts the corresponding radial positions of the particles at different moments of time. At $t = 0.2, 0.4$ and 0.6 s, the radial configuration of the nine particles exhibits only a small deviation from the inlet configuration, but after that the displacements of the particles from their initial positions are significant.

Table II presents the average axial velocities and the residence times of particles for Cases A1 and B. The range of the average velocities of the particles for Case B is much greater than that for Case A, showing that the inlet radial positions of particles significantly impact the residence time of particles in a helical pipe. The range of the residence times of particles for Case B is much greater than that for Case A1. The standard deviation of RTD in this case is 0.43 s compared to 0.20 s for Case A1, that is, the distribution of the residence time is more scattered, which can also be seen in Figure 12. It is observed in Figure 12 that the range of the residence time of particles is [1.2 s, 2.0 s] when the particles enter the pipe at the

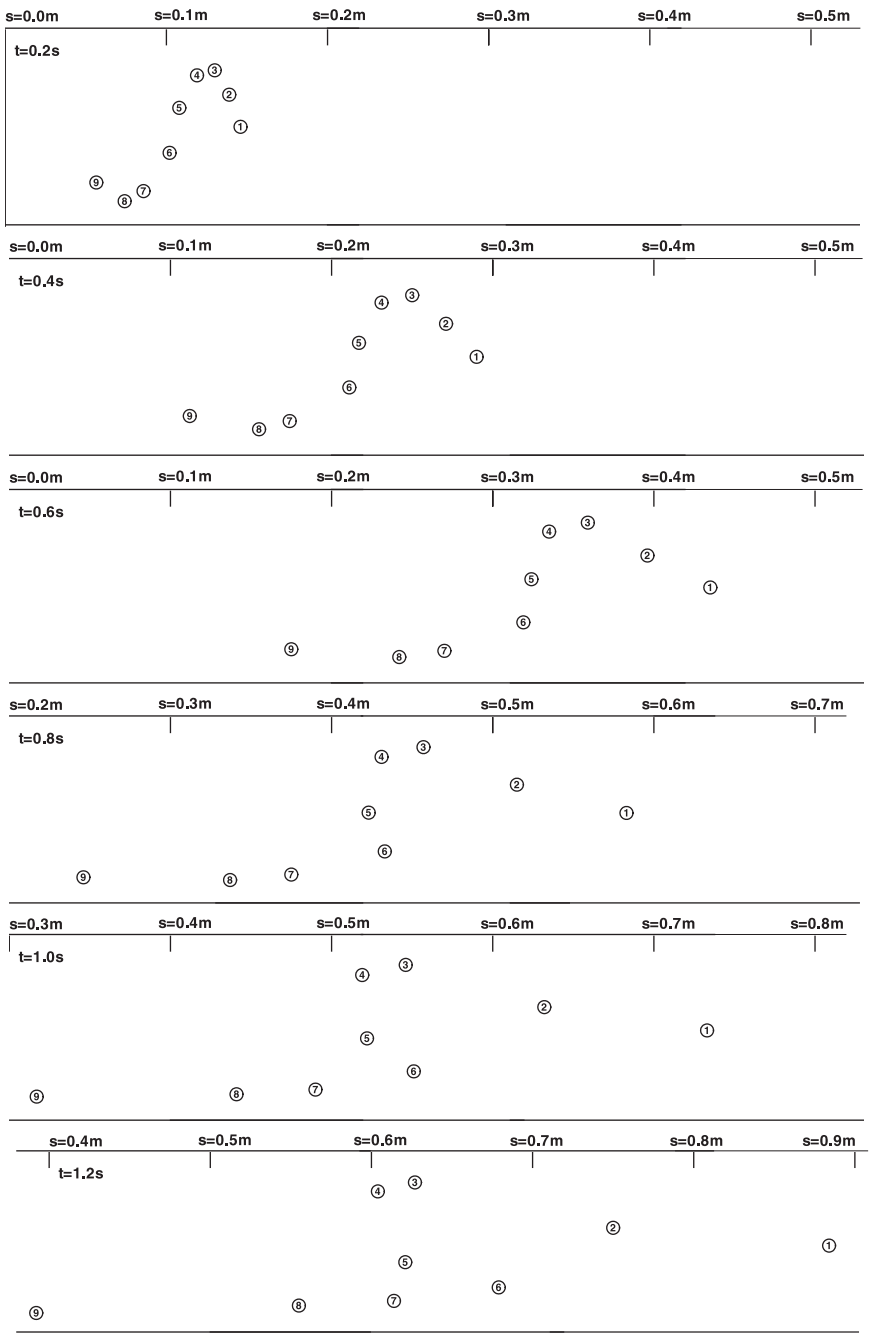

Figure 10. Snapshots of the particles at different moments of time (Case B).

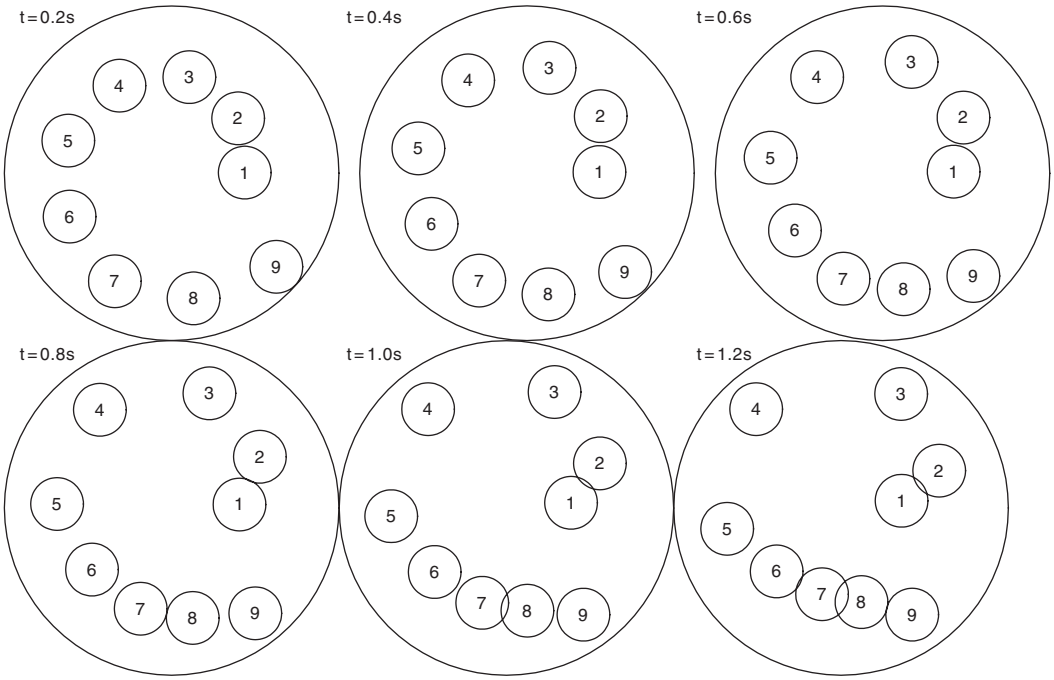

Figure 11. Radial positions of the particles at different moments of time (Case B).

Table II. Axial velocity and residence time of particles introduced to the inlet of the pipe at different inlet radial positions, computed for the mean flow velocity of $U_{s,\mathrm{f}} = 0.5\,\mathrm{m\,s^{-1}}$.

	Same radial position (Case A1)		Different radial positions (Case B)	
Particle No.	$U_{s,\mathrm{p}}(\mathrm{m\,s^{-1}})$	RT(s)	$U_{s,\mathrm{p}}(\mathrm{m\,s^{-1}})$	RT(s)
1	0.75	1.33	0.74	1.35
2	0.69	1.46	0.61	1.64
3	0.63	1.58	0.45	2.23
4	0.55	1.80	0.38	2.70
5	0.55	1.83	0.44	1.98
6	0.65	1.53	0.59	1.68
7	0.68	1.45	0.56	1.75
8	0.76	1.33	0.53	1.86
9	0.77	1.25	0.41	2.43
$\mathrm{RT}_{\mathrm{mean}}$		1.50		2.70
$\mathrm{RT}_{\mathrm{min}}$		1.83		1.35
$\mathrm{RT}_{\mathrm{max}}$		1.25		1.96
$\mathrm{RT}_{\mathrm{std}}$		0.20		0.43

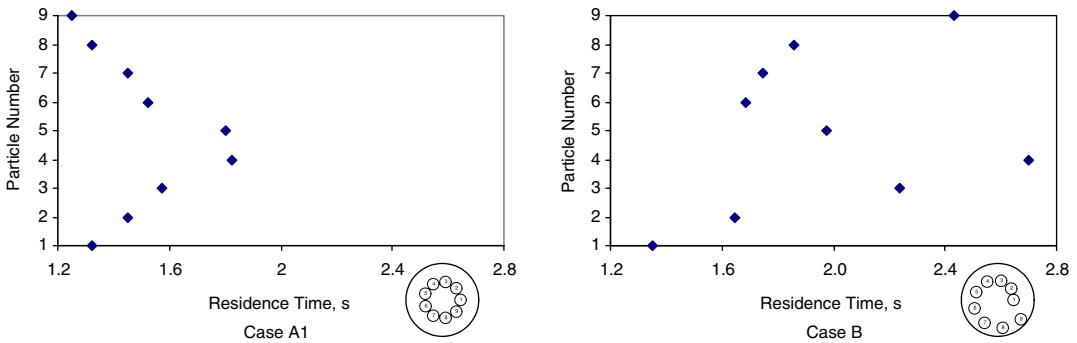

Figure 12. Residence time distribution of the particles introduced to the inlet of the pipe with the same mean flow velocity at the same radial positions (Case A1) and at different radial positions (Case B).

same radial position, while the range of the residence time is [1.2 s, 2.8 s] when the particles enter at different radial positions.

CONCLUSIONS

A flow model is developed to simulate a two-phase 3D flow of a non-Newtonian fluid in a helical pipe with large particles. The governing equations for the fluid flow in an orthogonal helical coordinate system are derived. The forces acting on the particles are analysed. The influence of the particles on the fluid is described by adding a source term to the momentum equation for the fluid flow. The source term is computed utilizing the force-coupling method. The particle–particle and particle–wall interactions are taken into account. It is shown that the particles have a significant effect on the flow field, including the axial velocity distribution and the strength of the secondary flow. The trajectories and velocities of the particles are predicted. The residence time distribution (RTD) of particles is analysed. It is shown that when the fluid axial velocity decreases, the mean residence time, minimum residence time, maximum residence time, and standard deviation of the residence time increase. When the particles are initially placed at different radial positions at the inlet of the pipe, the distribution of the residence time is more scattered than that for the case of the same inlet radial positions.

It is well known [22–24] that in Poiseuille flow in a straight pipe, neutrally buoyant particles collect at a preferred radial location. This phenomenon, called the Segre–Silberberg effect, is attributed to the nonlinear influence of inertia, and occurs due to the wall effects, velocity profile curvature, and shear force. Computational results presented in this paper do not indicate the existence of this phenomenon in Poiseuille flow in a helical pipe. Further research and numerical simulations performed using finer meshes and larger number of particles is needed to give a definitive answer on whether centrifugal forces and secondary flow in a helical pipe indeed destroy the Segre–Silberberg effect or it can be observed under special conditions.

NOMENCLATURE

a	pipe radius, m
a_{p}	particle radius, m
D_{p}	region occupied by a particle
$\mathbf{f}$	source term induced by particles, $\mathrm{N\,m^{-3}}$
$\mathbf{F}$	force, N
$\mathbf{F}_{\mathrm{b}}$	buoyancy force, N
$\mathbf{g}$	gravity, $\mathrm{m\,s^{-2}}$
$\mathbf{G}$	force dipole, N m
h_s, h_r, h_θ	scale factors associated with orthogonal coordinates s, r, θ, defined in Equation (3)
m	consistency factor, $\mathrm{Pa\,s^n}$
m_{f}	mass of the fluid in a finite volume, kg
m_{p}	particle mass, kg
n	power-law index
N	number of particles
p	pitch, m
P	pressure, Pa
Pr	Prandtl number
Re_{P}	particle Reynolds number
r	radial coordinate, m
R	coil radius, m
s	axial coordinate, m
t	time, s
$\mathbf{v}$	velocity vector, $\mathrm{m\,s^{-1}}$
$\mathbf{v}_{\mathrm{f}}$	fluid velocity, $\mathrm{m\,s^{-1}}$
$\mathbf{v}_{\mathrm{p}}$	particle velocity, $\mathrm{m\,s^{-1}}$
u_s, u_r, u_θ	velocity components, $\mathrm{m\,s^{-1}}$

Greek letters

β	declining angle
ε_{p}	stiffness parameters for particle–particle interactions, $\mathrm{m^3\,N^{-1}}$
ε_{w}	stiffness parameters for particle–wall interactions, $\mathrm{m^3\,N^{-1}}$
θ	angle
κ	curvature, $\mathrm{m^{-1}}$
μ	effective dynamic viscosity of a non-Newtonian fluid, $\mathrm{kg\,m^{-1}\,s^{-1}}$
ν	kinematic viscosity, $\mathrm{m^2\,s^{-1}}$
$\mathbf{\Omega}$	angular velocity vector, $\mathrm{s^{-1}}$
ρ_{f}	fluid density, $\mathrm{kg\,m^{-3}}$
ρ_{p}	particle density, $\mathrm{kg\,m^{-3}}$
τ	torsion, $\mathrm{m^{-1}}$
σ	length scale for force monopole, m
σ'	length scale for force dipole, m

Subscripts

s axial direction
r radial direction
θ tangential direction

Superscripts

p particle to particle
w wall to particle

ACKNOWLEDGEMENTS

The authors gratefully acknowledge the support of this work by a USDA grant. The authors are indebted to the reviewers for their constructive comments and suggestions.

REFERENCES

1. Shah RK, Joshi SD. Convective heat transfer in curved ducts. *Handbook of Single-phase Convective Heat Transfer*, Chapter 5. Wiley: New York, 1987.
2. Cheng L, Kuzentsov AV. Investigation of a laminar flow of a non-Newtonian fluid in a helical pipe. *International Journal of Applied Mechanics and Engineering*, 2005, in press.
3. Cheng L, Kuznetsov AV. Heat transfer in a laminar flow of a non-Newtonian fluid in a helical pipe. *International Journal of Transport Phenomena* 2004; **6**:293–306.
4. Liu Y, Zuritz CA. Mathematical modeling of solid–liquid two phase tube flow: an application to aseptic processing. *Journal of Food Process Engineering* 1995; **18**:135–163.
5. Durst F, Milojevic D, Schonung B. Eulerian and Lagrangian predictions of particulate two-phase flows: a numerical study. *Applied Mathematical Modeling* 1984; **8**:101–115.
6. Hu HH. Direct simulation of flows of solid–liquid mixtures. *International Journal of Multiphase Flow* 1996; **22**:335–352.
7. Johnson A, Tezduyar T. Simulation of multiple spheres falling in a liquid-filled tube. *Computational Methods in Applied Mechanics and Engineering* 1996; **234**:351–373.
8. Glowinski R, Pan TW, Hesla TI, Joseph DD. A distributed Lagrange multiplier/fictitious domain method for particulate flows. *International Journal of Multiphase Flow* 1999; **25**:755–794.
9. Fogelson AL, Peskin CS. A fast numerical method for solving the three-dimensional Stokes equations in the presence of suspended particles. *Journal of Computational Physics* 1988; **79**:50–69.
10. Sulsky D, Brackbill JU. A numerical method for suspension flows. *Journal of Computational Physics* 1991; **96**:339–368.
11. Maxey MR, Patel BK, Chang EJ, Wang P. Simulation of dispersed turbulent multiphase flow. *Fluid Dynamics Research* 1997; **20**:143–156.
12. Maxey MR, Patel BK. Localized force representations for particles sedimenting in Stokes flow. *International Journal of Multiphase Flow* 2001; **27**:1603–1626.
13. Lomholt S, Maxey MR. Force-coupling method for particulate two-phase flow: Stokes flow. *Journal of Computational Physics* 2003; **184**:381–405.
14. Sandeep KP, Zuritz CA, Puri VM. Modeling non-Newtonian two-phase flow in conventional and helical-holding tubes. *International Journal of Food Science and Technology* 2000; **35**:511–522.
15. Germano M. On the effect of torsion on a helical pipe flow. *Journal of Fluid Mechanics* 1982; **125**:1–8.
16. Germano M. The Dean equations extended to a helical pipe flow. *Journal of Fluid Mechanics* 1989; **203**: 289–305.
17. Liu D, Maxey M, Karniadakis GE. A fast method for particulate microflows. *Journal of Microelectromechanical Systems* 2002; **11**(6):691–702.
18. Bird RB, Stewart WE, Lightfoot EN. *Transport Phenomena* (2nd edn). Wiley: New York, 2002.
19. Dance SL, Maxey MR. Incorporation of lubrication effects into the force-coupling method for particulate two-phase flow. *Journal of Computational Physics* 2003; **189**:212–238.
20. Patankar SV, Spalding DB. A calculation procedure for heat, mass and momentum transfer in three-dimensional parabolic flows. *Journal of Heat and Mass Transfer* 1972; **15**:1787–1806.

21. Tanyel Z. Residence time distribution of multiphase particles in four configurations of holding tubes. *Master Thesis*, North Carolina State University, Raleigh, NC, 2004.
22. Matas JP, Morris JF, Guazzelli E. Inertial migration of rigid spherical particles in Poiseuille flow. *Journal of Fluid Mechanics* 2004; **515**:171–195.
23. Mortazavi S, Tryggvason G. A numerical study of the motion of drops in Poiseuille flow. Part I. Lateral migration of one drop. *Journal of Fluid Mechanics* 2000; **411**:325–350.
24. Matas JP, Glezer V, Guazzelli E. Trains of particles in finite-Reynolds-number pipe flow. *Physics of Fluids* 2004; **16**:4192–4195.

